Towards adapting reverse vertical seismic profiling for ambient-noise imaging with transient sources

Automatic estimation of stationary-phase receivers for improved retrieval of the interferometric Green's function

Chamarczuk, Michał; Draganov, Deyan; Quiros, Diego; Malinowski, Michał

DOI
10.1190/geo2021-0293.1

Publication date
2022

Document Version
Final published version

Published in
Geophysics

GEOPHYSICS, VOL. 87, NO. 6 (NOVEMBER-DECEMBER 2022); P. KS169–KS182, 10 FIGS.
10.1190/GEO2021-0293.1

DOI:10.1190/geo2021-0293.1

Towards adapting reverse vertical seismic profiling for ambient-noise imaging with transient sources: Automatic estimation of stationary-phase receivers for improved retrieval of the interferometric Green's function

Michał Chamarczuk[1], Deyan Draganov[2], Diego Quiros[3], and Michał Malinowski[4]

ABSTRACT

Most of the ambient-noise studies are performed with sensor arrays located at the surface. Passive recordings containing seismic arrivals from subsurface sources could be seen as having a geometry resembling reverse vertical seismic profiling (RVSP). In such scenarios, the intersource seismic-interferometry technique can be used to redatum the surface receivers to the subsurface source positions resulting in virtual shot gathers at depth. The success of the interferometric processing primarily requires that a correlation panel created in the interferometric process contains stationary-phase regions that, when summed, retrieve events with correct timing, whereas nonstationary contributions are canceled. We have addressed the combination of the RVSP configuration and ambient-noise measurements. We develop a prototype of a data-driven technique allowing us to adapt the summation process such that changes in the stationary-phase requirements imposed by changes in the noise-sources distribution can be adaptively satisfied without the need for array redeployment. We propose to identify the receivers located in the stationary-phase regions by scanning for stationary contributions in the correlation panel prior to stacking. Our method uses the correlation coefficient and time windowing to distinguish between stationary and nonstationary arrivals. The improved Green's function estimate is obtained by limiting the summation to only those receivers that, when summed, enhance the stationary and attenuate the nonstationary contributions. We test this using a simple 2D numerical example to find a practical way to alleviate insufficient receiver coverage. We determine the theoretical possibility to improve the intersource Green's function estimates without explicit knowledge of the target and the source distribution. However, our data-driven approach has the disadvantage of being limited to scenarios in which the correlation panel from all receivers contains identifiable stationary-phase arrivals.

INTRODUCTION

In its most general form, seismic interferometry (SI) is a method used to estimate the acoustic or elastic Green's function between two locations. Early field examples of SI estimated parts of the Green's function between two receivers by crosscorrelating their cotemporal records (e.g., Shapiro et al., 2005), with deconvolution or cross coherence used as an alternative to crosscorrelation in some cases (e.g., Nakata et al., 2011). The trace retrieved by SI represents the wavefield that would have been recorded at one of the receivers had there been a source at the location of the other (Wapenaar, 2004). Because no actual source is required at either receiver, the term virtual source is generally used to distinguish it from real seismic sources. This type of SI is known as interreceiver interferometry, and as the name suggests, it retrieves the wavefield between two or more receiver pairs (Figure 1a and 1b). A different type of SI, known as intersource interferometry, was proposed by Curtis et al. (2009) in which the Green's function between two sources can be retrieved. The goal of intersource interferometry is to retrieve a virtual receiver (VR) recording at one source location that would have been generated by the other source (Figure 1c and 1d).

In SI, the seismic energy used to create virtual records can be generated by various types of sources, such as controlled sources

Manuscript received by the Editor 7 May 2021; revised manuscript received 14 June 2022; published ahead of production 2 August 2022; published online 22 September 2022.
[1]Rice University, Earth, Environmental, and Planetary Sciences, Houston, Texas, USA. E-mail: chamarczukm@gmail.com (corresponding author).
[2]Delft University of Technology, Faculty of Civil Engineering and Geosciences, Delft, The Netherlands. E-mail: d.s.draganov@tudelft.nl.
[3]University of Cape Town, Department of Geological Sciences, Cape Town, South Africa. E-mail: diego.quirosugalde@uct.ac.za.
[4]Institute of Geophysics PAS, Warsaw, Poland and Geological Survey of Finland, Espoo, Finland. E-mail: michalm@igf.edu.pl.

DOI:10.1190/geo2021-0293.1

(Bakulin and Calvert, 2004; Schuster et al., 2004; Draganov et al., 2007a), (micro) earthquakes (Curtis et al., 2009), train and vehicle traffic (Nakata et al., 2011; Quiros et al., 2016), industrial processes (Miyazawa et al., 2008), and ambient seismic noise (Lin et al., 2007; Cheraghi et al., 2015; Polychronopoulou et al., 2020). The latter, which can be thought of as encompassing background noise generated by natural phenomena (e.g., ocean wave action) and human activity (e.g., mining and urban activities), has been successfully used with SI to retrieve surface and body waves responses, including body-wave reflections in different environments and with different survey geometries (e.g., Draganov et al., 2009; Zhan et al., 2010).

In mining environments, reflection imaging has been used to explore for gold, platinum, and base metal deposits across the globe (e.g., Durrheim, 1986; Milkereit et al., 1996; Malehmir and Bellefleur, 2009; Manzi et al., 2012), with most of the surveys using standard recording geometries, with sources and receivers arranged in surface arrays. In some cases, where higher resolution of the target is needed or there are specific illumination requirements (e.g., steeply dipping structures), borehole seismic methods are used, including crosshole imaging and vertical seismic profiling (VSP) surveys (e.g., Pretorius et al., 2011). A VSP survey is generally described as one in which either the source or the receivers are deployed down a borehole (Hardage, 2000) and can potentially record using 1D (e.g., surface source next to borehole), 2D (e.g., linear source array), and 3D (e.g., 2D source array) geometries. A particular type of a VSP experiment, in which sources are placed down a borehole and receivers are placed at the surface, is known as a reverse VSP (RVSP) survey (Figure 1e). The raypath geometry of an RVSP survey is essentially the same as what is found in mine environments when receivers are placed at the surface to monitor underground mine activity, such as mine bursts, seismicity, and mine stability, with the added complication of not knowing precisely the location of these sources (e.g., Quiros et al., 2017). One approach to image structures in a mine environment would be to locate these events (assuming that their amplitude is above the background noise level and arrivals are impulsive), and subsequently apply RVSP processing to obtain a reflection profile or volume in the case of 2D receiver arrays at the surface (e.g., Quiros et al., 2015a, 2015b). However, if these events are difficult or impossible to identify in seismic records, a better approach is to consider them part of the local ambient noise and use SI to retrieve body-wave reflections and subsequently obtain a structural image.

Applications of SI in mineral exploration are not as ubiquitous as in other areas of seismology such as petroleum exploration, anthropogenic seismology, and large-scale crustal imaging (Draganov et al., 2007b; Lin et al., 2008; Quiros et al., 2016). Nonetheless, examples of SI applied to mining environments exist which focus on ambient-noise tomography with surface arrays (e.g., Hollis et al., 2018; Chen et al., 2021; Liu et al., 2022), retrieval of body waves between receivers deployed at depth (Olivier et al., 2015), and reflection imaging using ambient noise (e.g., Chamarczuk et al., 2017, 2018, 2021; Polychronopoulou et al., 2020).

In this study, we address the specific combination of having an RVSP acquisition geometry, with sources treated as identifiable and separable arrivals within the recorded ambient noise, and its transformation into an entirely subsurface geometry (Figure 1f) using intersource SI (Curtis et al., 2009), and a new dedicated processing methodology for the improvement of Green's function retrieval.

As previously mentioned, many seismic data sets in mineral exploration resemble the RVSP geometry, in which the receivers are placed at the surface to record underground activity. For this scenario, the intersource SI methodology proposed by Curtis et al. (2009) facilitates the transformation of the RVSP geometry into a subsurface geometry in which VRs are created at different source positions at various depths. Explicitly, via intersource SI, the responses are retrieved between pairs of sources by summation over the receivers at the surface. This approach has several advantages over the interreceiver SI method; for instance, it provides responses that can produce detailed images of deeper targets (Tonegawa and Nishida, 2010). In addition, the intersource SI approach is especially suitable for ambient-noise studies (with transient-source responses in them) because it allows improvement of the retrieved results by manipulation of the receiver array while reducing the need for controlled sources, especially in areas with challenging terrain or locations that are logistically inaccessible.

A key concept in SI is that of the stationary-phase approximation, an important method in the field of asymptotic analysis (Bender and Orszag, 1999; Bleistein, 2012). For the case of interreceiver geometry (Figure 1a and 1b), the main contribution to the retrieved Green's function

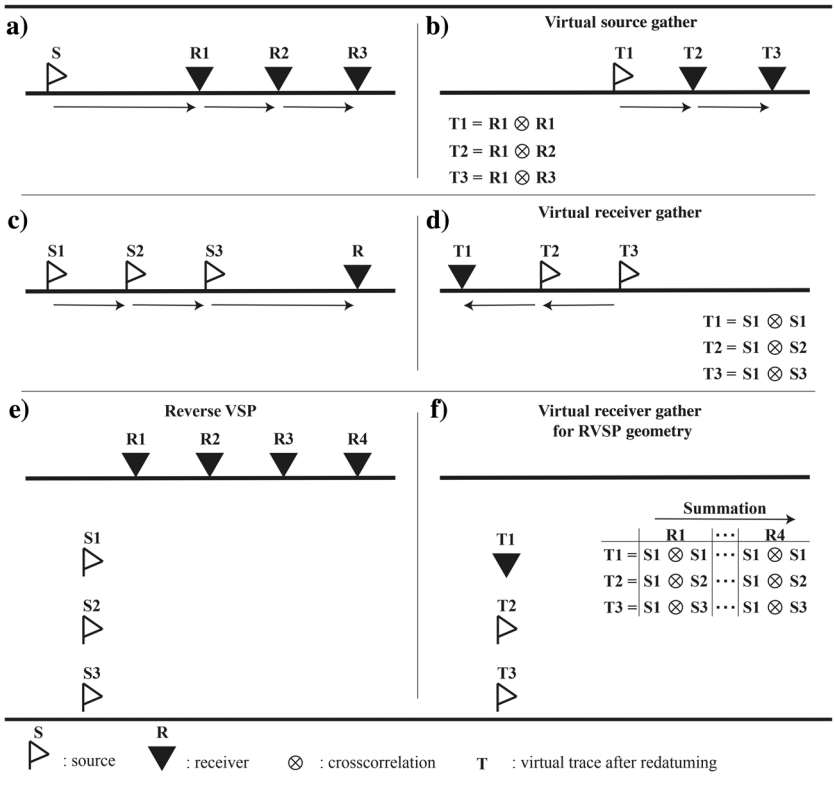

Figure 1. Diagrams of source-receiver geometries used for different SI configurations and their processing outcomes: (a) interreceiver geometry, (b) virtual-source gather retrieved for the geometry in (a), (c) intersource geometry, (d) VR gather retrieved for the geometry in (c), (e) RVSP geometry, and (f) VR gather retrieved for the geometry in (e).

DOI:10.1190/geo2021-0293.1

comes from sources located along rays that reach two target receivers by passing first one of them and then the other (e.g., surface source inline with two receivers), and those in the Fresnel zone around these sources (Snieder, 2004). We refer to these sources as stationary-phase sources. Importantly, if the correlation gathers created in the SI processing contain a stationary-phase region, the summed or stacked correlation gather will retrieve (at least kinematically) correct seismic arrivals while reducing the contributions from nonstationary components.

Just as with interreceiver SI, the stationary-phase region is paramount in retrieving the desired arrivals (i.e., direct arrivals and reflections) with intersource SI (Hong and Menke, 2006; Curtis et al., 2009; Saengduean et al., 2021). In intersource SI, the summation of correlated responses is over receiver positions, meaning that the stationary-phase requirements depend on the receiver-array aperture and spatial sampling. Practically, it means that the summation limits depend on the receiver aperture, and the integration points depend on the receiver spacing. In certain field scenarios, such as a time-constrained ambient-noise survey or for areas with limited sources at depth (i.e., induced or natural), one could have more receivers than sources, which would allow to easily capture the stationary points when summing over the receivers (Liu et al., 2014, 2016). Nevertheless, sufficient spatial distribution of receiver positions is still required to obtain (kinematically) accurate intersource Green's functions (Curtis et al., 2009; Tonegawa and Nishida, 2010; Draganov et al., 2012).

During ongoing data-acquisition campaigns with ambient-noise recordings (e.g., in mining camps, Cheraghi et al., 2015) or with temporary arrays recording aftershocks (Quiros et al., 2015a), there is no spatial or temporal control over the source location. In these cases, the optimal location of receivers will dynamically change, requiring near real-time processing to satisfy the rapidly changing stationary-phase requirements.

The solution we present next, which we call automatic selection of stationary-phase receivers (ASPRE), is a simple data-driven technique that identifies and rejects the nonstationary contributions from a specific receiver. Although our approach addresses intersource SI with an RVSP configuration, our method is generally applicable to a wide range of SI configurations. In the next sections, the applicable details of SI will be reviewed and the ASPRE algorithm will be explained and tested on an idealized synthetic data set.

MOTIVATION

To effectively extract the Green's function between two sources, it is necessary to consider the size of the stationary-phase region at the surface and the distribution of the receivers. Here, we focus on alleviating the receiver-coverage problem and investigate the effects of limiting the spatial summation over receiver positions to improve the accuracy of the retrieved Green's function. ASPRE automatically identifies receivers located in stationary-phase regions by scanning for stationary contributions in the correlation panel and preserving only those crosscorrelation functions (CCFs), which contain in-phase arrivals in the time window of expected energy (e.g., reflected arrivals). To understand how ASPRE works and where it fits in the processing sequence, we first describe the conventional processing workflow for RVSP data via intersource SI (Figure 2a). The first step in the conventional workflow is to create a common-receiver gather (CRG) for all sources. Next, one cross-correlates the source at the VR position with each source in the CRG. This is followed by resorting the correlated data into common crosscorrelated source pairs, which created correlated panels over receiver positions. Finally, summation over all receiver positions results in a retrieved Green's function.

From the processing point of view, the correlation panel C can be viewed as the basic building block, which should be preprocessed before stacking (Poliannikov and Willis, 2011). Consequently, the correlation panel can be viewed as a 2D matrix whose dimensions are time lags from crosscorrelations and receivers (Melo et al., 2013), in which the Green's function is retrieved by stacking the correlation panel along the receiver dimension. When the minimum acquisition criteria are not met, for example, due to gaps in coverage or by large receiver spacing, the conventional "brute" stacking will introduce artifacts or spurious arrivals (Draganov et al., 2006; Poliannikov and Willis, 2011). In particular, for the intersource SI, Tonegawa and Nishida (2010) suggest that to improve the retrieved Green's function, the adopted stacking process should minimize the bias of the inhomogeneous distribution of receivers. To directly address this issue, and to try to improve the conventional processing sequence, we introduce the ASPRE methodology (Figure 2b), which can be applied before stacking along the receiver dimension.

Our technique relies on the assumption that most events that are in phase (i.e., minimal moveout) along the receiver dimension in the correlation panel result from receivers in stationary-phase locations. These stationary arrivals contribute to forming the intersource Green's function, and as such might be detected after stacking the correlation panel. Nonstationary signals are characterized by incoherent, out-of-phase events contributing to hindering the retrieval

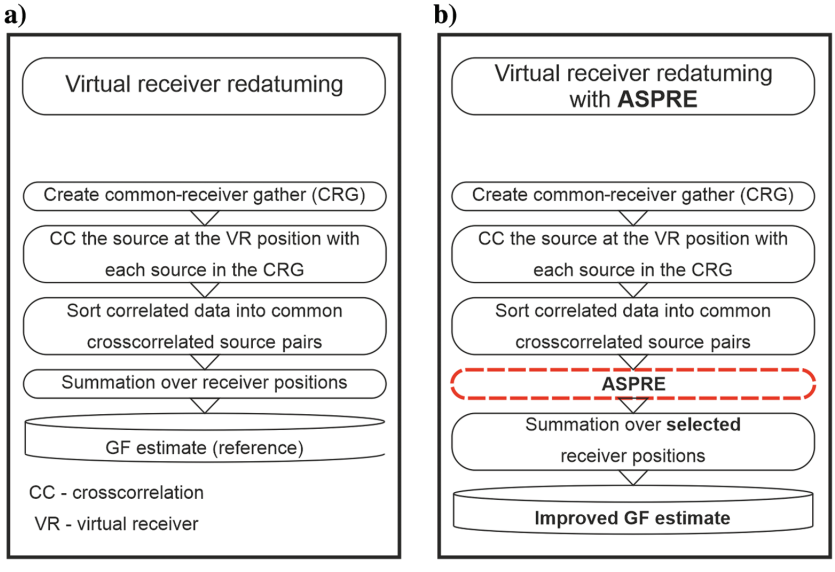

Figure 2. Processing workflows for generating VR data. Workflows differ in the summation processing step. (a) The conventional VR redatuming workflow involves summation over all available receivers. (b) The modified workflow includes the additional ASPRE processing step, which aims to select only receivers in the stationary-phase regions, and the subsequent summation is over selected receiver positions.

of clear physical arrivals during the summation process (Mehta et al., 2007). Assuming complete receiver coverage, these out-of-phase arrivals will likely cancel out in the summation, and they might be detected only before stacking by analyzing the CCFs forming the correlation panel at hand. From this, we determine the stationarity of a signal based on the similarity of the current CCF inside the correlation gather to the stacked Green's function obtained from summing over all available receiver positions. To measure similarity, we use a correlation coefficient.

In the next sections, we go into detail about the processing steps involved in ASPRE and focus on a theoretical approach to answer the question of whether the adoption of selective stacking to minimize the bias of an inhomogeneous receiver distribution can be achieved in an automatic way by using solely a data-driven approach.

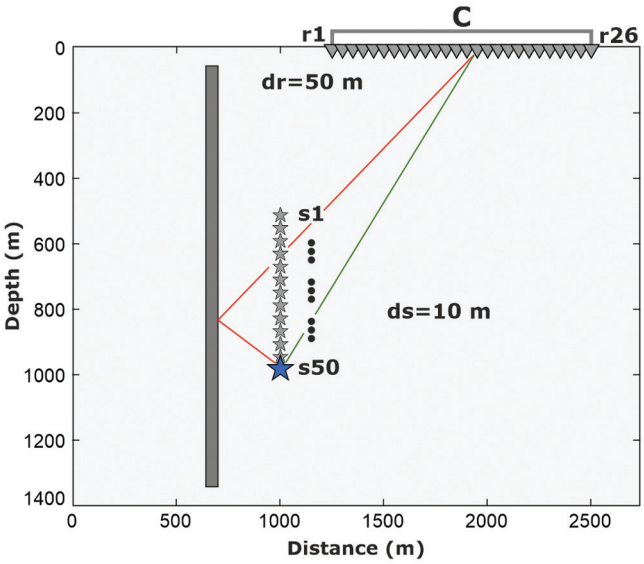

Figure 3. Source-receiver geometry for the acoustic synthetic example simulating an RVSP acquisition geometry. The background medium and the vertical target are homogeneous with velocities of 5800 and 6200 m/s, respectively. There are 50 sources (stars) located along a vertical line and 26 receivers (triangles) located at the surface. For display purposes, each 5th source is plotted. Raypaths for a direct (green) and a reflected (red) arrival are shown. The bold capital letter **C** indicates the set containing all receivers.

VR	Common receiver 1	+	Common receiver 2	+	Common receiver 3	...	Common receiver 26	=	VR gather
1	$S_1 \otimes S_1$	+	$S_1 \otimes S_1$	+	$S_1 \otimes S_1$	...	$S_1 \otimes S_1$	=	$VR_1{:}S_1$
	$S_1 \otimes S_2$		$S_1 \otimes S_2$		$S_1 \otimes S_2$		$S_1 \otimes S_2$		S_2
	$S_1 \otimes S_3$		$S_1 \otimes S_3$		$S_1 \otimes S_3$		$S_1 \otimes S_3$		S_3
	⋮		⋮		⋮		⋮		⋮
	$S_1 \otimes S_{50}$		$S_1 \otimes S_{50}$		$S_1 \otimes S_{50}$		$S_1 \otimes S_{50}$		S_{50}
...	...		...		...	...	...		...
50	$S_{50} \otimes S_1$	+	$S_{50} \otimes S_1$	+	$S_{50} \otimes S_1$	...	$S_{50} \otimes S_1$	=	S_1
	$S_{50} \otimes S_2$		$S_{50} \otimes S_2$		$S_{50} \otimes S_2$		$S_{50} \otimes S_2$		S_2
	$S_{50} \otimes S_3$		$S_{50} \otimes S_3$		$S_{50} \otimes S_3$		$S_{50} \otimes S_3$		S_3
	⋮		⋮		⋮		⋮		⋮
	$S_{50} \otimes S_{50}$		$S_{50} \otimes S_{50}$		$S_{50} \otimes S_{50}$		$S_{50} \otimes S_{50}$		$VR_{50}{:}S_{50}$

$S_{50} \otimes S_2$: crosscorrelation of source 50 with source 2 $VR_{50}{:}S_{50}$: virtual receiver located at source position S_{50}

Figure 4. Processing scheme for creating VRs. Here, S_i represents the source number, where i corresponds to sources 1–50 in the RVSP configuration shown in Figure 3. Note that a VR is created at each source position, from 1 to 50, and the reader is reminded that only 26 receivers are present in the synthetic example.

SYNTHETIC MODEL AND METHODS

To demonstrate the idea behind our method, we use a model representing a 2D acoustic medium with a vertical target, receivers at the surface, and sources at depth along a vertical line (Figure 3). The model simulates an RVSP survey geometry, but we emphasize that the ideas and conclusions are general for all SI applications whenever the summation over an incomplete receiver boundary is involved. For simplicity, we assume a regularly distributed line of receivers placed on a flat surface, and straight, vertical line of sources parallel to the flat target flank. The target flank is perpendicular to the surface. This configuration approximates the practical acquisition geometry often used in ambient-noise studies with surface arrays (e.g., Draganov et al., 2013; Cheraghi et al., 2015; Nakata, 2016; Asgharzadeh et al., 2019; Dales et al., 2020). We use an idealized, almost unrealistic distribution of underground sources, which is however relevant to the presence of strong, localized sources often occurring in mining areas (for more details, see "Discussion" section).

We simulate seismic data using a fourth order in space and second order in time acoustic finite-difference forward-modeling scheme (Youzwishen and Margrave, 1999). The synthetic RVSP data generated for a minimum-phase 40 Hz Ricker wavelet are converted into VR data via inter-source SI.

Standard SI workflow

The detailed data-processing workflow required to redatum the RVSP data into VR data was shown in Figure 2a. This workflow is expanded for completeness in Figure 4, in which the redatuming of the RVSP data into a VR gather is shown as a table of crosscorrelations for each CRG (i.e., columns) and summation over the receiver dimension (i.e., rows), in which the final result — a VR at a particular source location (e.g., $VR_{50}{:}S_{50}$) — is given in the rightmost column.

Figure 5 shows modeled synthetic data and the intermediate computation steps used to obtain the VR gathers. The data are modeled as common-source gathers (i.e., recording of one source by all receivers) and they are shown in Figure 5a as the starting point of the processing workflow. We start by rearranging the data into CRGs (i.e., recording of all sources by one receiver), as shown in Figure 5b. Then, we obtain a subsurface virtual-source gather at the source location i (where $i = 1, \ldots, 50$ for our model) by crosscorrelating the trace that corresponds to the source i with every other trace (i.e., source) in the CRG. This procedure is repeated for every receiver position. The final step is the sorting of the crosscorrelated source pairs into correlation panels (i.e., rows in Figure 4) and stacking them (Figure 5c). Each stacked correlation panel produces one trace in the VR gather. After redatuming receivers to the source locations, we obtain the new seismic profile of sources and VRs oriented parallel to the target (see Figure 3).

Although Figure 5 shows the processing steps needed to generate a VR gather, in Figure 6, we show the visualization of transforming the VR

DOI:10.1190/geo2021-0293.1

gathers (Figures 5c and 6a) using selective stacking of the negative and positive time lags. The selective stacking is implemented due to the strong one-sided illumination present in the VR gathers, with the results shown in Figure 6b. In addition, a synthetic data set (Figure 6c) is generated using 50 sources and 50 receivers at the locations of the sources in Figure 3. This directly modeled data can be used for comparison with the final VR gathers to evaluate the performance of the intersource SI. The selective stacking is shown in greater detail in Figure 6d, where the semitransparent polygons indicate regions of the causal or acausal lags that are not used in the generation of the final VR gathers. For example, the VR for source position 1 (VR 1) uses only the positive lags of the gather, whereas the negative lags are discarded. Similarly, for source position 40, most of the negative lags contribute whereas only a small section of the positive lags contributes to the final VR gather VR 40. These final receiver gathers, for which four gathers (i.e., VR 1, 10, 40, and 50) are shown in Figure 6e, can be compared with the directly modeled results of Figure 6f. While comparing Figure 6e and 6f, a few arrivals should be commented on. First, the reflected arrival (with hyperbolic moveout) from the target is seen on the VR gathers and the directly modeled data, whereas the direct arrival is the most prominent arrival in both data. Additional arrivals with linear moveouts are seen in the VR gathers that are not present in the directly modeled data. These are artifacts resulting from the incomplete surface receiver coverage in Figure 3.

Having reviewed the standard processing workflow for creating a VR gather, we will now focus on the concept of stationary-phase regions and their importance for the ASPRE methodology.

Stationary-phase receivers

For each source pair in the model in Figure 3, a set of surface receiver locations exists that satisfies the required stationary-phase ray geometry for the target reflector (Brand et al., 2013). However, in practical applications, the precise reflector location will not be known, and thus the correct stationary-phase ray geometry cannot be predetermined. Conventionally, the intersource Green's function between two sources is obtained by crosscorrelating the signals generated by these two sources and summing over all available receiver positions. The bold capital letter **C** (not to be confused with correlation panel C) in Figure 3 denotes that the summation range is over the complete receiver boundary, which for our synthetic experiment is equivalent to 26 receiver positions.

As explained previously, the correlation panel $C(x_i, \tau)$ can be viewed as a 2D matrix. More specifically, it is an $N \times (2M - 1)$ matrix, with $2M - 1$ time samples (M is a number of samples prior to crosscorrelation) and N receivers. Here, C is formed by contributions from individual receivers; however, it also depends on the location of the given pair of sources. Because at the acquisition stage we do not have control over the present transient sources in the subsurface, we focus on improving the results on the receiver-array part.

The retrieved estimate of the Green's function between a pair of source locations at x_A and x_B is obtained by stacking the correlation gather C over the receiver dimension:

$$G = G(x_B, x_A, t) + G(x_B, x_A, -t) \approx \sum_{i=1}^{N} C(x_i, \tau), \qquad (1)$$

where τ denotes the correlation time lag. For clarity, the symbols x_A and x_B are left out of the correlation term on the right side of equation 1. Repeating this procedure for all source pairs (Figure 7) results in a VR gather at a particular source position. The inset in Figure 7a draws attention to the results retrieved between three source locations, where the blue triangle denotes a VR at source position S_{50}, whereas the green and red stars denote sources at positions S_{25} and S_1, respec-

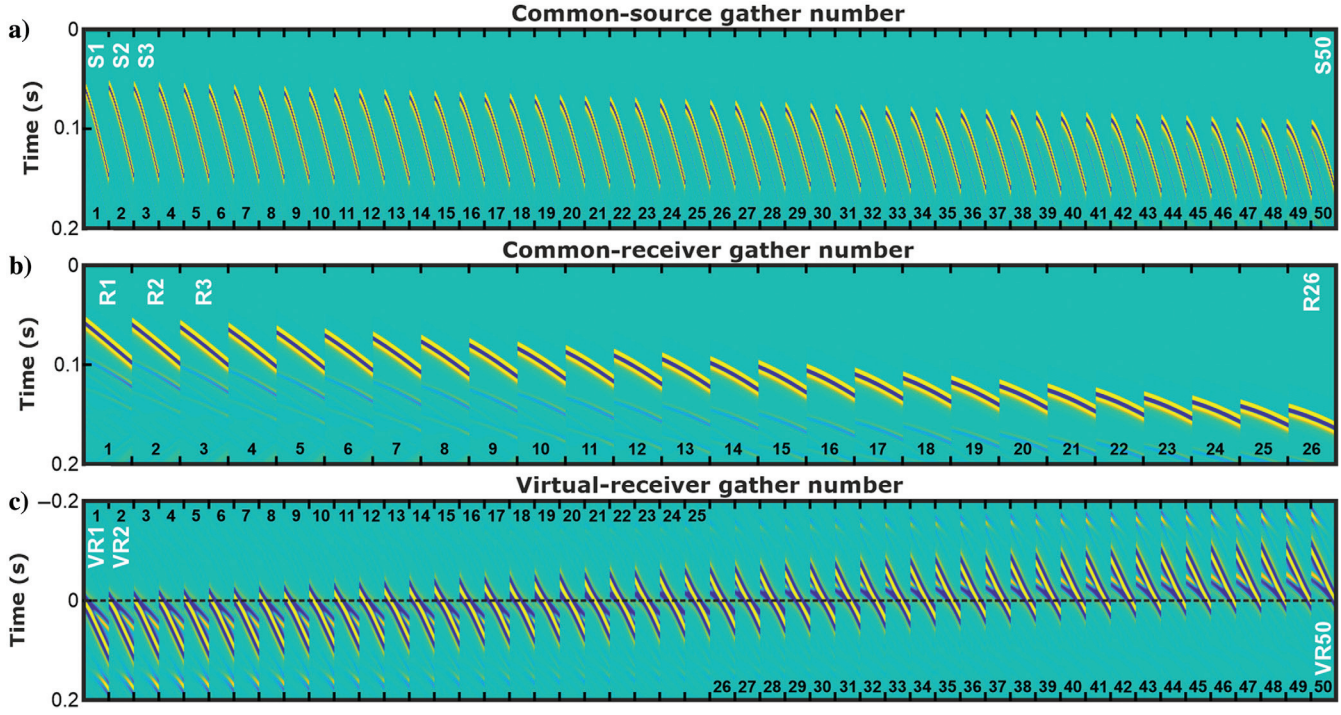

Figure 5. Processing scheme for retrieving VRs at each source position. (a) Synthetic data generated for the model in Figure 3 displayed as common-source gathers. (b) CRGs that result from rearranging the records in (a). (c) VR gathers retrieved at each source position (see Figure 4).

tively. The bold capital letter $\mathbf{C}'$ indicates the summation range over a subset of receivers; each subset will vary in number depending on the stationary-phase region. Figure 7b shows the VR gather for source position S_{50} (the blue triangle), with estimated Green's functions for sources S_{25} and S_1 indicated by green and red stars, respectively.

As mentioned previously, the constructive contribution in the correlation panel will come from receivers located in stationary-phase regions. With the limited receiver aperture though, the summation does not assure the removal by destructive interference of cross-talk events nor retrieval by constructive interference of physical arrivals. This means that, by stacking over the complete receiver interval $\mathbf{C}$, we might retrieve erroneous results. This is clearly visible in Figure 7b, in which the retrieved result obtained from stacking over the complete correlation panels C exhibits not only both kinematically correct arrivals but also artifacts.

Instead of adding more receivers in the field or redeploying the array, we propose to minimize artifacts retrieved from nonstationary arrivals and further enhance the prominence of stationary-phase arrivals by limiting the summation process to receivers yielding stationary arrivals, that is, those located in the stationary-phase region. In this approach, the improved Green's function G' is obtained by selective stacking:

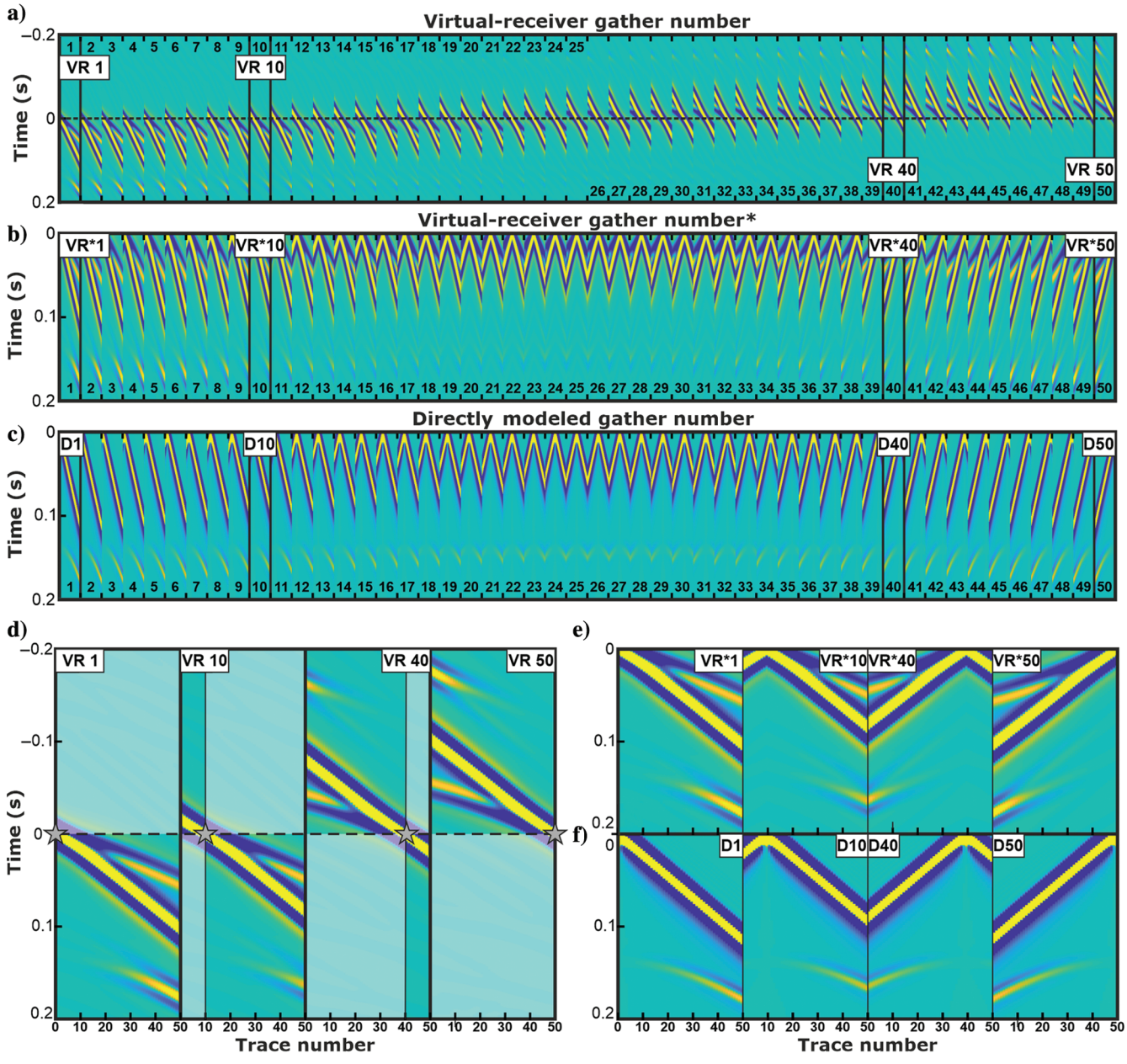

Figure 6. (a) VR gathers computed in Figure 5c with a few selected gathers (vertical black lines) for further analysis. (b) VR gathers after the selective stacking of positive and negative lags in (a). (c) Directly modeled data for 50 sources and 50 receivers collocated at the source locations in Figure 3. (d) Selective stacking of positive and negative lags of the VR gathers in (a). The regions in semitransparent polygons are discarded (deselected) and do not contribute to the final VR gather. (e) The final VR gathers for VR 1, 10, 40, and 50. (f) Directly modeled gathers corresponding to the gathers in (e).

$$G'(x_B, x_A, t) \approx \sum_{j}^{P} C'(x_j, \tau), \tag{2}$$

where C' represents a subset of the original correlation panel C, obtained by extracting rows corresponding to the receivers in the discrete stationary-phase regions. The subset of receivers used to form C' is denoted with $\mathbf{C}'$ in Figure 7a. The new limit of summation is denoted by P, where $P \leq N$, because the number of receivers used for summation in the selective stacking is generally smaller than the number of all available receivers used in the conventional stacking in equation 1. Note that $G'(x_B, x_A, t)$ in equation 2 is still an estimate of the true Green's function, and, as it will be explained subsequently, it may be erroneous due to the use of a restricted set of receivers.

Before introducing the detailed processing steps of ASPRE, we discuss the use of selective stacking in the correlation panel, which can be thought of as the simplest form of ASPRE. The receivers used in the stacking boundary (or stacking contour) $\mathbf{C}'$ may be selected through different criteria such as visual inspection or numerical metrics.

The example of a VR gather obtained with such selective stacking is shown in Figure 7c. Each trace in Figure 7c results from using a subset of receivers, where each subset can vary in size. This is illustrated by the stacking boundaries in Figure 7a (i.e., $\mathbf{C}'$). Each color-coded boundary corresponds to the set of receivers selected to retrieve the Green's function among three particular source pairs (S_{50}–S_{50}, S_{50}–S_{25}, and S_{50}–S_1). In such a scenario, the selection of receivers toward the improved Green's function G' can be expressed using a weight vector:

$$G' = \sum_{=1}^{N} w(x_i) C(x_i, t), \tag{3}$$

where w denotes a binary weight vector, with $w = 0$ for nonstationary receivers and $w = 1$ for stationary-phase receivers:

$$w(x_i) = \begin{cases} 1, & x_i \in \mathbf{C}' \\ 0, & x_i \notin \mathbf{C}' \end{cases}, \tag{4}$$

where $\mathbf{C}'$ is the subset of receivers that have been determined to contribute physical arrivals to the retrieved interstation Green's function. The Green's functions obtained from stacking CCFs of receivers belonging to $\mathbf{C}'$ contain the in-phase reflection and direct arrivals and are less contaminated with artifacts (compare Figure 7b and 7c). It must be noted that, for the synthetic scenario shown in Figure 7a, all arrivals in the positive time lags are artifacts. However, because the overall number of artifacts is reduced (compare Figure 7b and 7c), we argue that, in general, the result is enhanced. For the purpose of this study, the preceding improvement is sufficient.

To automate the process of receiver selection, we need to update the weight values of w in a data-driven way. Toward this end, we investigate the correlation panels for the three Green's function estimates highlighted with colors in the inset of Figure 7a and shown as the blue, green, and red traces in the VR gathers in Figure 7b. Figure 8 shows the CCFs of the three colored Green's functions in Figure 7b. Each horizontal trace in the correlation panels shown in Figure 8b, 8d, and 8f corresponds to the CCF for a fixed source pair and a particular receiver position. The top panels in Figure 8 highlight the estimate for G and improved estimate G' of the retrieved Green's function. We show the correlation panels to explain that only some receivers can contribute constructively to the specific arrivals in the final estimates of G'. For the purpose of this explanation, artifacts are arrivals in G' (e.g., Figure 8a) that should sum destructively in the correlation panel (e.g., Figure 8b), but due to the limited receiver aperture, they do not.

The question we now pose is whether it is possible to automatically assess the similarity between G obtained from stacking over all receivers (e.g., Figure 8a) and the respective individual CCFs forming the correlation panel (e.g., Figure 8b). One way to objectively measure the similarity between time series is by computing their CC (Jones and Morrison, 1954). We expect to obtain increased CC values for those receivers which contribute to nonartifacts visible in the reference estimate G.

The results for the CC are shown in Figure 8g, where the coefficients are computed between the trace G and each trace in the corresponding correlation panel (e.g., trace G in Figure 8a and each trace in Figure 8b). The highest CC values in Figure 8g correspond to traces included in the stacking boundaries highlighted with the capital letter $\mathbf{C}'$ (e.g., Figure 8d), where the respective colored lines correspond to the red, green, and blue subsets indicated in Figure 8b, 8d, and 8f, respectively. It is from the sum of CCFs in these subsets that the improved Green's function G' is estimated.

However, using a whole-trace CC is an imperfect metric because the CC reflects only the average similarity between traces. As noted previously, our aim is to pinpoint receiver positions contributing in-phase stationary arrivals at a particular lag time. This is illustrated by the arrivals within the green polygon in Figure 8b, in which several of these arrivals would be expected to contribute to the reflection retrieval. Note that only receivers which yield CCFs with arrivals approximately in phase with the reference arrival in trace G should contribute constructively during the summation process. For example, arrivals corresponding to receivers 1–3 and 24–26 within the green polygon (time window) are clearly out-of-phase with the corresponding arrival in G (Figure 8a), whereas arrivals

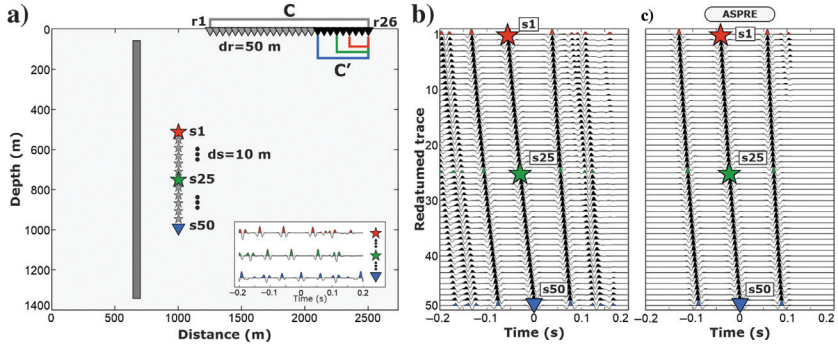

Figure 7. (a) Source-receiver geometry as described in Figure 3. Here, $\mathbf{C}'$ indicates a subset of receivers. The blue triangle denotes the location of the VR, whereas the green and red stars denote source locations that will be used to evaluate the correlation panels in Figure 8. The inset shows the Green's function estimates for source pairs S_{50}–S_{50}, S_{50}–S_{25}, and S_{50}–S_1. (b) The VR gather at source position S_{50}, with Green's functions for source position S_{25} and S_1 denoted with green and red stars, respectively. (c) The VR gather at source position S_{50} generated with the selective stacking methodology.

for receivers 6–13 are clearly in phase. It becomes clear that the way to automatically identify correctly contributing receivers requires analyzing CCFs in time windows targeted at specific arrivals, rather than using a whole-trace CC. ASPRE is an attempt to implement a quasiautomatic approach that uses objective metrics (e.g., CC within narrow time windows and selective stacking) to select stationary-phase arrivals in a data-driven way.

The analysis of the results in Figure 8 indicates the following stationary-phase details that should be considered during the intersource SI processing and the development of ASPRE: (1) in-phase contributions (stationarity) should be evaluated for individual arrivals, (2) the subset of stationary-phase receivers depends on the location of the sources in a pair, and (3) a single CCF in a correlation panel may contain in-phase and out-of-phase events for different time lags.

ASPRE

The ASPRE workflow can be viewed as the processing module in the modified VR redatuming method, in which the conventional summation along the receiver boundary is adapted for (1) maximizing the in-phase contributions from reflection arrivals and (2) minimizing artifacts. In Figure 2b, we show the placement of ASPRE within the conventional workflow, in the following sections, the processing steps forming the core of ASPRE are described in detail. As will be explained, the core components of ASPRE are selective stacking, time-windowing, and CC computation. Of these components, the latter two are tunable processing steps and demand a trial-and-error approach for choosing the optimal parameters. We use our simple and idealized synthetic experiment to illustrate the generic ASPRE procedure. In real-world case studies, it is up to the data processor to replicate the performance of ASPRE using the general rules of thumb showcased here.

Time windowing and CC

To understand the relevance of time-windowing and CC computation, we once again consider Figure 8. As explained previously, the colored lines in Figure 8g represent the CC values when using whole traces, which include useful events (in-phase arrivals) and artifacts (out-of-phase arrivals). Figure 8b and 8g also shows the stacking contour $\mathbf{C}'_{\mathbf{R}}$, which highlights eight receivers (denoted by green dots in Figure 8b) that show high similarity with G ($|CC| > 0.9$) when considering the green time window and poor similarity ($|CC| < 0.6$) when considering entire traces (Figure 8g). Furthermore, the arrivals (high-amplitude peaks) for these eight receivers within the green window also are in closest agreement with the theoretical onset expected for the reflection off the model target (Figures 3 and 7a). This suggests that, when the stacking contours $\mathbf{C}'$ and $\mathbf{C}'_{\mathbf{R}}$ are compared for effectiveness in retrieving the reflection arrival within the green time window, one can conclude that ASPRE is improved by using the windowing approach versus a whole-trace correlation analysis. This superiority comes from using the CC within predetermined time windows, which allows to clearly pinpoint the receiver positions contributing constructively to a retrieved arrival.

The selection of target time windows can be addressed in several ways, and it is used in diverse seismological studies; for a thorough overview of time-windowing methods and applications, see Perron et al. (2018). In our data-driven approach, we assume a minimum

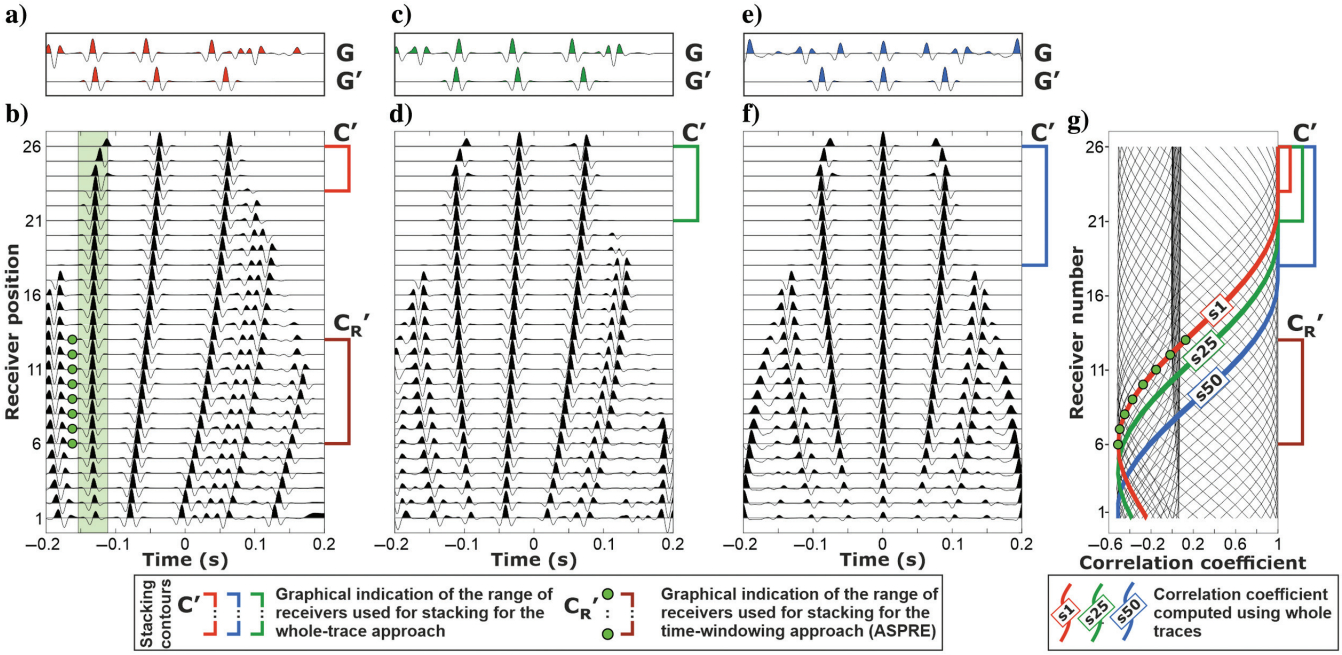

Figure 8. (a) Green's function estimated for source pair S_{50}–S_1 using all receivers G (same as an inset in Figure 7a) and a subset of receivers G'. (b) Correlation panel for source pair S_{50}–S_1 using all available receivers. The green semitransparent polygon (window) highlights a particular arrival. Here, $\mathbf{C}'$ and $\mathbf{C}'_R$ indicate different subsets of CCFs. (c) Same as in (a) but for source pair S_{50}–S_{25}. (d) Same as in (b) but for source pair S_{50}–S_{25}. (e) Same as in (a) but for source pair S_{50}–S_{50}. (f) Same as in (b) but for source pair S_{50}–S_{50}. (g) Stationary-phase analysis using the CC measured between the reference estimate G shown in the top panels (a, c, and e) and each trace of the corresponding correlation panel (b, d, and f), respectively. Green dots denote receivers in the stationary-phase region for the reflection retrieval obtained with the ASPRE methodology (based on the time-windowing and CC computation discussed in the next sections). The CCs obtained with ASPRE are not plotted in (g), and the green dots indicate high CC within the window in (b) and the G trace in (a).

knowledge about the geology and the location of the identified transient sources in the noise recordings. The practical implementation of the ASPRE workflow for a single source pair is shown in Figure 9. The basic assumption guiding our processing is that the estimate G obtained from stacking over all available receiver positions could be used as a reference to determine the approximate range of time lags of stationary arrivals. In this way, we can measure the quality of the SI results without a priori knowledge of the geometry of the target and sources.

The time-window selection can be implemented in several ways depending on the characteristics of G. Given that our synthetic example provides a G trace that is relatively clean and with good temporal separation between high-amplitude events, we decide to first use the event with a positive peak at roughly −0.06 s to divide the trace G into two sections, one to the left and one to right from the reference peak. We then automatically select five (this number is arbitrary and can be increased or decreased) large positive peaks to the left and right of the reference peak (numbers 1–10 in Figure 9a panel I). Next, we separate the odd number peaks (blue triangles in Figure 9a panel $\mathrm{II_A}$) from the even number peaks (green triangles in Figure 9a panel $\mathrm{II_B}$). The time lags of the odd and even peaks are used to create two sets of time windows (black vertical lines). The temporal size of the windows in panel $\mathrm{II_A}$ is indicated by the horizontal pointers with two arrowheads within the blue-shaded polygon. Similarly, the size of the windows in panel $\mathrm{II_B}$ is shown by the horizontal pointers within the green-shaded polygon. The gray-color sections in panels $\mathrm{II_A}$ and $\mathrm{II_B}$ indicate parts of the trace not included in the windows. Since we are interested in the retrieval of reflected arrivals, we select the trace in panel $\mathrm{II_B}$ because one of its windows completely captures the reflected arrival peaking at roughly −0.12 s. This selected trace is plotted in Figure 9a panel III, with the reflection highlighted by the green-shaded time window, and it serves as our reference windowed Green's function to compare with each of the traces in the correlation panel (Figure 9b, panel IV). Finally, we create the input for ASPRE by rejecting the receivers with nonstationary contributions and preserving those with high correlation values (denoted with $\mathbf{C}'_{\mathbf{R}}$ in Figure 9b panel VI).

Panel IV in Figure 9b shows a time section (−0.2 to 0.03 s) of the correlation panel of Figure 8b, where the traces are color-coded and superimposed on the trace from panel III (dashed black line). The color coding represents the value of the CC between the CCF for each receiver and G within each of the selected time windows (1–5) as defined by the color-scale bar in Figure 9b. Window 2 is shown as a green-shaded polygon, and it contains a reflection arrival. Panel V shows this same window magnified, where it is clearly visible that increased deviations from the reference trace G correspond to low CC values (the blue tones), whereas traces with little deviation from G correspond to high CC values (the red tones). Panel VI shows the actual values of the CCs computed from V (the thick black line), whereas it also shows the CCs computed using the whole-trace approach (the dashed red line, also shown in Figure 8g as a solid red line). The stacking contour $\mathbf{C}'_{\mathbf{R}}$ indicates the range of receivers identified to have a CC value equal to or larger than a predetermined threshold value ($R_{\mathrm{thresh}} \geq 0.7$ in our example). These receivers identified by the ASPRE approach will be used in obtaining an improved Green's function G'_R for the analyzed time window. The stacking contour $\mathbf{C}'$, as discussed previously in the text, represents the range of receivers identified using the CC values calculated for whole traces. Notice the drastic difference in the two stacking contours, and how ASPRE with time windowing has a superior behavior in selecting receiver positions that satisfy stationarity with respect to the reference Green's function. Following the ASPRE methodology for all source pairs (each source pair has a correlation panel that must be analyzed) results in an improved VR gather (e.g., Figures 7c and 9b). Figure 9c shows the main steps in the ASPRE processing as discussed in this section, and Figure 9d shows all symbols used in Figure 9b.

The ASPRE-improved Green's function G'_R can now be written using a weight matrix based on normalized CC values and time windowing:

$$G'_R = \sum_i^N \sum_k^T w(x_i, \tau_k) C(x_i, \tau_k). \tag{5}$$

The weight vector w is now dependent on receiver position and time (i.e., w is now a matrix) where T represents the number of time windows used to analyze a correlation panel, whereas k is the index of the time window. The elements of the weight matrix remain binary as compared with equation 4, and they are assigned based on the value of the normalized CC:

$$w_{ik} = \begin{cases} 1, & |R_{ik}| \geq R_{\mathrm{thresh}} \\ 0, & |R_{ik}| < R_{\mathrm{thresh}} \end{cases}, \tag{6}$$

where $|R_{ik}|$ represents the absolute value of the normalized CC for ith receiver and the kth window, whereas R_{thresh} denotes the CC threshold value empirically chosen. The latter determines whether a receiver contributes constructively to a refection retrieval for a particular time window, or if it should be discarded.

Specifically, any $|R_{ik}|$ values below the threshold indicate receivers outside the stationary-phase region $\mathbf{C}'_{\mathbf{R}}$, and which should be rejected from the stack. As an alternative approach to equation 6, which is a data-driven binary selection, it is possible to use more data, by directly using the values R_{ik} without thresholding:

$$w_{ik} = |R_{ik}|, \tag{7}$$

Practically, this means that $|R_{ik}|$ value can be used to multiply each row of C before stacking. In this approach, which we do not explore further, more data can be used to produce the improved retrieved Green's function, while still prioritizing the rows of C with the strongest stationary components.

Stationary-phase receivers selection panel

In Figure 10, we show the ASPRE evaluation for every other source pair within the time window of interest shown in Figure 9b (the green-shaded polygon). In other words, Figure 10a shows the same analysis as the one shown in panel V in Figure 9b but repeated for every other source used in the model with source $\mathrm{S_{50}}$ as the VR position. Notice that panel V, which has the receiver number as the vertical axis in Figure 9b, is rotated 90° clockwise and placed at the top of Figure 10a. Similarly, for every other source pair, the same windowed section of the correlation panel is extracted for each receiver and plotted in the horizontal direction. The color intensity reflects the value of R_{i2}, where index 2 indicates the time window under analysis (Figure 9b; equation 5). We can now use this graphical display to design the stacking contour based on the region of high correlation values. This

contour is denoted with a gray line in Figure 10a and outlines the receiver positions which are located in the stationary-phase region for the reflection event. The result shown in Figure 10a represents the practical implementation of selective summation for reflection retrieval. The main idea behind Figure 10a is to demonstrate how the ASPRE works, and although the results evaluated in Figure 10a are obtained from a very simple synthetic example, the intention is for it to serve as a proof of concept.

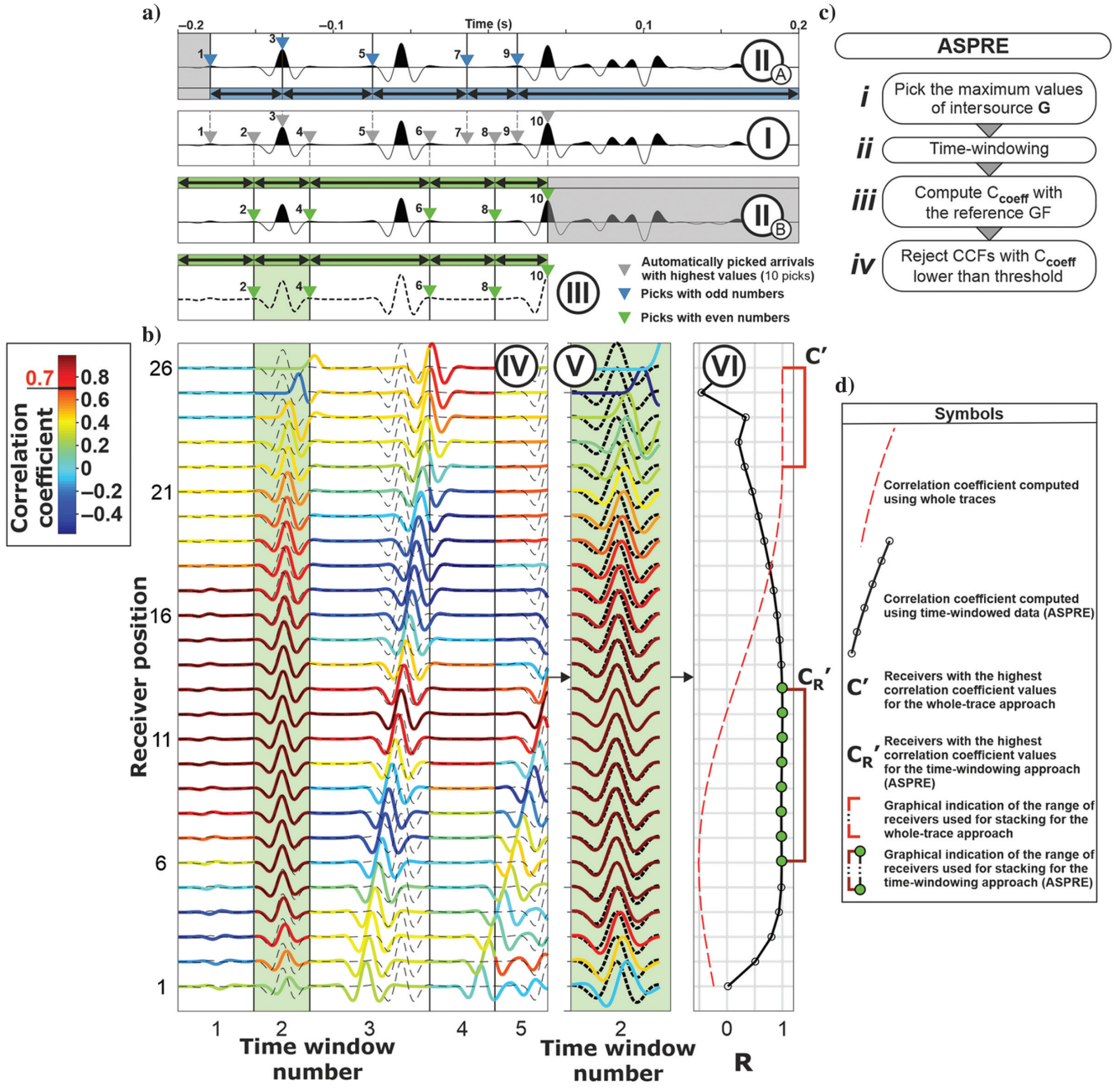

Figure 9. (a) Green's function estimate from stacking all available receivers is shown in the panel I (same as Figure 8a, trace *G*). The gray triangles numbered 1–10 indicate selected positive peaks left and right of the reference positive peak at roughly −0.06 s. Panels II_A and II_B show the same trace *G* as in panel I, but with different time windows created based on the odd (1, 3, 5, 7, and 9) and even (2, 4, 6, 8, and 10) peaks, respectively. Horizontal arrows within the blue and green-shaded regions in panels II_A and II_B, respectively, show the size of the created time windows. Panel III shows the trace G divided into the windows that will be used for comparison with the correlation panel. Note that the trace is shown as a dashed line. The green-shaded window contains a reflection of interest. (b) Panel IV shows the correlation panel (colored lines) from Figure 8b with a superimposed trace from panel III (dashed black line). The color represents the CC value between the two traces in each window (see color-scale bar). Panel V shows a magnified version of the window of interest (window 2 in panel IV) where the phase shift at traces 1–3 and 24–26 is more easily visible. Panel VI shows the CC computed for window 2 in panels IV and V (black line), while also showing the CC values computed with the whole-trace approach (dashed red line). The stacking contours $\mathbf{C}'_{\mathbf{R}}$ and $\mathbf{C}'$ referred to in the text also are shown. (c) Detailed workflow of ASPRE. (d) Symbols used in (b).

DOI:10.1190/geo2021-0293.1

Figure 10b illustrates the surface receiver locations required to obtain a valid VR gather at source position S_{50} via the ASPRE methodology for every other source pair. The stationary-phase arrivals extracted following the procedure shown in Figure 9 indicate that, for the shallower source positions, the contribution results solely from far offsets, whereas the arrivals extracted for the deeper source positions result from the broad range of receiver locations.

DISCUSSION

The acquisition geometry used in most of the ambient-noise studies with surface arrays resembles the RVSP configuration, in which a single receiver line or array of receivers records the local ambient noise. For reflection retrieval, only sources of body waves, ideally relatively deeper in the subsurface, are needed. Recorded ambient noise could contain such sources, as microseismicity in mining areas, and that sort of source is targeted in our study. When such identified sources are located in the direct vicinity of subsurface targets, it is tempting to use the benefits of intersource SI. However, the usual receiver geometry and the temporal and spatial changes of the target sources limit the quality of the SI results. We have presented a prototype of a data-driven approach to address the incomplete receiver boundary and varying stationary-phase regions at the surface. In the following, we discuss the advantages and disadvantages of our approach, some of its limitations, and how it could be further improved to tackle real-world scenarios.

Advantages and disadvantages of ASPRE

As shown previously, the ASPRE methodology is capable of retrieving an improved Green's function G'_R when compared with the reference Green's function G obtained from the model in Figure 3. The results suggest that this approach is advantageous when compared with the standard workflow of stacking all available data. In addition, there are aspects of the ASPRE workflow that can be modified to serve the characteristics of the data at hand, for example, certain parameters can be tuned (e.g., the threshold CC), whereas others (e.g., the window selection) could be implemented in the frequency domain or based on certain characteristics of the waveforms (e.g., the lowest frequency of interest). The methodology is not computationally intensive, at least in its current form, and can be implemented with limited resources.

As mentioned previously, our methodology relies on the assumption that events that are in phase along the receiver dimension in the correlation panel correspond to physical arrivals in the retrieved Green's function. However, we note here that stationary arrivals also can contribute potentially equal amounts of energy to nonphysical arrivals in the SI Green's function estimates (e.g., van Manen et al., 2005; Draganov et al., 2012). If the receiver boundary is closed, these will cancel out, but if it is not, then they will remain (e.g., Löer et al., 2014; Meles et al., 2015). In the presence of strong intrinsic energy losses, nonphysical arrivals will be retrieved even in the case of a closed boundary (Draganov et al., 2010). In other words, the stack over all receivers, which in the current version of implementing ASPRE is used as the reference (e.g., Figure 9a), may contain nonphysical arrivals. In such cases, ASPRE will still keep such arrivals as they are characterized by a stationary-phase region.

Another potential negative consequence of applying ASPRE, is the possibility to enhance artifacts, instead of physical energy. In our simple synthetic example, it is easy to focus the analysis on the correct reflected arrival, whereas with field data it might be more difficult, because of the impossibility to distinguish which arrivals are physical, and which are artifacts. Using a priori information about expected arrival times of events could alleviate this problem to a certain degree. Thus, the synthetic example and demonstration of ASPRE performance presented in this study should be considered as a simple, almost unrealistic, but canonical example that demonstrates the principle of the data-driven adjustment of an array of receivers to the distribution of identified subsurface sources.

Tunable parameters of ASPRE

We showed that using our methodology, one can improve the estimated Green's function by a simple data-driven approach in situations when the receiver boundary has limited dimensions. From the acquisition point of view, the only requirement for our method is that there are more receivers inside the stationary-phase regions than outside, so that during summation the amplitudes of the physical arrivals (reflections) outweigh the artifacts. Thus, our method is a generic tool for improving the intersource Green's functions. However, to achieve the best performance, it is important to tune the following parameters: the location of the target window, values for the weight vector, and the CC selection threshold. These parameters can be estimated by the standard trial-and-error approach and

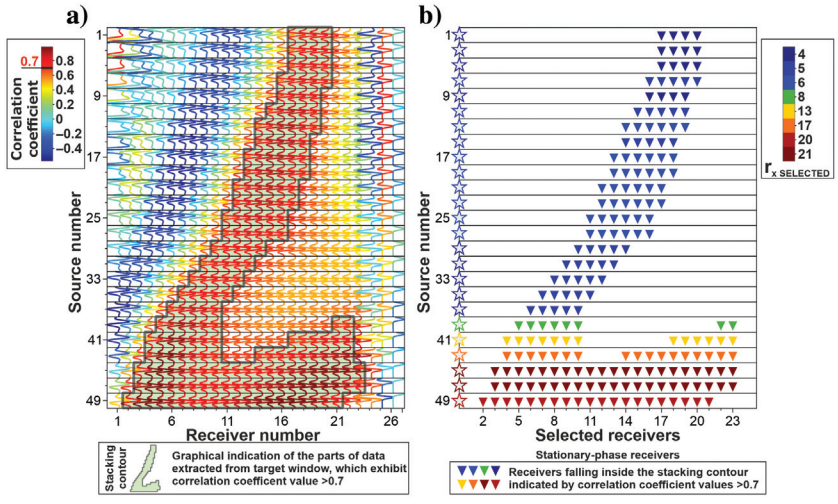

Figure 10. Practical implementation of ASPRE for a VR at source position S_{50}. (a) Matrix representation for the correlation panel of every other source pair at time window 2 (see Figure 9b panel IV). Row 1 corresponds to source pair S_{50}–S_1, and this is the same as Figure 9b panel V but rotated 90° clockwise. The color indicates the normalized CC value measured between G and every trace in the correlation panel (horizontal dimension) for every other source pair. The gray line denotes the stacking contour separating data below and above the threshold value ($R \geq 0.7$) and used to single-out receiver stations contributing with stationary components. (b) Receiver positions selected via ASPRE for every other source pair as shown in (a). The color scheme represents the number of receivers used for a particular source pair. The color scheme is shown on the right.

DOI:10.1190/geo2021-0293.1

visual inspection using the graphical panels shown in Figures 9 and 10. The final choice of the target time window is up to the user, but, as explained previously, the summation over all receivers will eventually converge to the result in which the stationary contributions are dominant; thus, the selection of a proper time window could be guided by choosing time intervals with the highest correlation value. For example, the target window in panel IV in Figure 9b clearly exhibits the highest amplitudes (greater than 0.7 of the maximum CC) compared with the remaining windows. For the same reason, using the estimated Green's function retrieved from stacking over all receiver positions as the initial reference is a good practical choice. For future case studies, we note here that the criteria for the time windowing are not arbitrary. When dividing the reference trace into two subsets (see panels II_A and II_B in Figure 9), we choose the subset which entirely captured the arrival we wanted to enhance. Comparing panels II_A and II_B in Figure 9a, we can see that arrival we targeted in this case (denoted with a green transparent polygon in panels III and IV in Figure 8a and 9) was better captured by the even set of picks (denoted with green triangles in Figure 9a); therefore, it is further used for CC analysis in Figure 9b. In other words, the choice of proper time windowing is dictated by which set of time windows better preserves the arrivals of interest.

The choice of the weights vector can be approached in at least two ways: by directly using the normalized CC values (equation 7) or with a binary approach making use of a threshold value (equation 6). The weights vector should typically be set by the decision maker, a possibility would be to make the sum of all weights equal to one and each w_{ik} greater than zero for a particular time window k. If the weights are not normalized, then the sum of the weights need not add to one. The latter offers more stable results, as any outliers possibly caused by poor coupling or local noise could be alleviated.

Limitations of ASPRE

Although the focus of this paper is on a data-driven improvement of the SI results, it is important to be aware of the acquisition and geologic limitations constraining the retrieval of the kinematically correct intersource Green's function estimate. Accurate imaging of a complex target requires an optimal field design aimed at minimizing the spatial aliasing in the correlation panel and thus assuring good constructive and destructive interference in the summation process. The success of imaging with the sources identified in the noise recordings with surface arrays would depend on the source and receiver spacing, the total number of sources and receivers, source aperture, reflector distance from the identified sources, and background velocity. Furthermore, the effects of the forward scattering associated with spatially complex geologic heterogeneities and the size of targets may potentially contribute to an increase in the range of propagation angles that may produce unexpected stationary-phase rays. Hurich and Deemer (2013) show that, by using the ray-tracing method to understand the limitations of realistic acquisition scenarios, it is possible to produce an optimal virtual-source image of steeply dipping targets. Nevertheless, as highlighted in that study, the ray tracing does not address the question of whether the wavefield is sampled sufficiently to form the kinematically correct virtual gathers. In particular, it is not clear whether the source spacing (in our case the receiver spacing) is sufficient to avoid spatial alias in the correlation panel.

The applicability of ASPRE is highly case-dependent due to the inherent requirement of having a sufficiently dense sampling of the correlation panel (i.e., of the surface receivers) to ensure constructive and destructive interference. In cases such as hard-rock environments, e.g., mining camps, the relatively high subsurface velocities effectively mitigate this issue as they would allow relatively course receiver sampling. This makes the application of ASPRE in such environments justified.

On the other hand, a specific feature of mining environments is the presence of many strong, localized sources of body waves such as underground mine excavations and blasts, open-pit mine blasts at the surface, trains, and heavy machinery which can be very advantageous for imaging with intersource SI, and thus for application of ASPRE.

Specific applications of ASPRE

The applicability of the RVSP geometry applied in conjunction with intersource SI allows to redatum surface receivers to subsurface VR locations as dictated by the locations of the identified transient sources in the recorded ambient noise. If the sources are distributed sub vertically and the target has a subvertical orientation, this geometry lends itself to common-midpoint reflection processing and imaging because the VRs and underground sources would have a common datum and would be subparallel to the target (Brand et al., 2013; Hurich and Deemer, 2013). Imaging steeply dipping targets with common-midpoint processing of virtual profiles is an especially appealing method for mining-camp environments because they often are characterized by access restrictions and steeply dipping targets. Brand et al. (2013) show that interreceiver SI applied to the conventional VSP data allows redatuming surface shots to borehole receiver locations and the consecutive imaging of nearly vertical targets. A further improvement of this approach would be to replace the costly surface walk-away shots with a receiver array and use the transient subsurface sources generated by the underground mine for the VR redatuming combined with ASPRE.

It has been proven that the RVSP configuration combined with ambient-noise recordings is a powerful tool for imaging of subsurface targets using aftershocks (Quiros et al., 2017). This is particularly appealing for ASPRE as it involves the processing of rapidly evolving clusters of events, which change spatially and temporally.

Intersource SI also has been successfully applied to the global-scale seismology (e.g., Curtis et al., 2009), and crustal seismology (Tonegawa and Nishida, 2010), to retrieve arrivals between pairs of earthquakes. Of particular interest for seismologists is the capability of intersource SI to estimate the Green's function between deep earthquakes associated with subducting slabs. Few studies report successful utilization of specific arrivals in the recorded ambient noise for imaging of the structural complexity of subduction slabs (Nishitsuji et al., 2016; Casas et al., 2020) especially for the oceanic lithosphere. It is known that the seismicity of slabs is associated with clusters of earthquakes occurring in the Wadati-Benioff zones, which are located along subvertical planes of the lithosphere descending into the upper mantle (e.g., Zhang et al., 2019). APSRE could be used for processing of the recorded noise data from temporary or permanent arrays of seismometers deployed at the surface in the vicinity of slabs. Specifically, our methodology would theoretically allow evaluating and using the stationary-phase earthquakes associated with the slab without the need for redeploying the stations and consequently used as the monitoring tool of the slab activity.

Further improvement of the methodology

A necessary improvement of ASPRE is addressing the complicated nature of ambient-noise sources typical for the given study area. For instance, strong seismic sources present in the mining areas (underground mine excavations and blasts, open-pit mine blasts on the surface, trains, and heavy machinery, among others) with varying magnitude and complex waveforms can be processed via cross coherence to equalize source characteristics (Place et al., 2019) for the intersource imaging.

Finally, it is important to note that, in this study, we focus specifically on the reflection arrival because our method is aimed to facilitate reflection imaging. However, the same approach could be used for choosing receivers in stationary-phase regions for other types of arrivals identified in cross correlograms. For instance, ASPRE could enhance the estimation of trapped waves used in imaging of the fault zones (Ben-Zion et al., 2003; Hillers et al., 2014).

CONCLUSION

We propose a data-driven methodology for the ASPRE for the application of intersource SI with surface receiver arrays and transient subsurface sources present in ambient-noise recordings. The ASPRE method singles out receivers located in the stationary-phase regions by scanning for in-phase contributions in the correlation panel formed by the correlation of recordings at the receivers from a transient source. Using numerically modeled data for a simple and idealized subsurface model, we showed how to reject the nonstationary contribution based on the similarity between data-derived reference Green's function and individual traces in the correlation panel for a source pair. This showed the theoretical possibility to improve the processing results from continuously recording surface arrays by adjusting the summation process to the dynamic changes in the stationary-phase requirements. Future research should use more complicated models to extend the applicability of the ASPRE methodology and to demonstrate its practical applications beyond the proof of concept we showed here. Our study was devoted to an initial, theoretical approach to answering the question of whether the spatiotemporal changes of transient sources identified in ambient-noise recordings can be alleviated by automatic selection of receivers using a data-driven approach. This question was only partially answered because the simplistic synthetic example we used did not assure that ASPRE will successfully tackle structurally complicated real-world scenarios. For this reason, at the current stage of development, ASPRE can be used only in specific scenarios, for example, when the stack from all receivers contains identifiable stationary-phase arrivals. Further research is needed to evaluate ASPRE on more complex structural models, in which the stack over all receivers may contain many artifacts but also nonphysical arrivals.

ACKNOWLEDGMENTS

The manuscript was significantly improved thanks to comments from assistant editor A. Guitton, associate editor C. Birnie, reviewers K. Mehta and M. Asgharzadeh, and four anonymous reviewers. The corresponding author thanks for the discussions with N. Nakata, M. Chamarczuk and M. Malinowski were supported by the National Science Center (Poland) grant no. UMO-2018/30/Q/ST10/00680 (FULLIMAGE project).

DATA AND MATERIALS AVAILABILITY

Data associated with this research are available and can be obtained by contacting the corresponding author.

REFERENCES

Asgharzadeh, M., A. Grant, A. Bona, and M. Urosevic, 2019, Drill bit noise imaging without pilot trace, a near-surface interferometry example: Solid Earth, **10**, 1015–1023, doi: 10.5194/se-10-1015-2019.

Bakulin, A., and R. Calvert, 2004, Virtual source: New method for imaging and 4D below complex overburden: 74th Annual International Meeting, SEG, Expanded Abstracts, 2477–2480, doi: 10.1190/1.1845233.

Bender, C. M., and S. Orszag, 1999, Advanced mathematical methods for scientists and engineers I: Asymptotic methods and perturbation theory. Vol. 1: Springer Science & Business Media.

Ben-Zion, Y., Z. Peng, D. Okaya, L. Seeber, J. G. Armbruster, N. Ozer, A. J. Michael, S. Baris, and M. Aktar, 2003, A shallow fault-zone structure illuminated by trapped waves in the Karadere-Duzce branch of the North Anatolian Fault, western Turkey: Geophysical Journal International, **152**, 699–717, doi: 10.1046/j.1365-246X.2003.01870.x.

Bleistein, N., 2012, Mathematical methods for wave phenomena: Academic Press.

Brand, E., C. Hurich, and S. Deemer, 2013, Geometrical considerations in the acquisition of borehole interferometric data for imaging near-vertical features: Design of field experiments: Geophysics, **78**, no. 3, K1–K10, doi: 10.1190/geo2012-0171.1.

Casas, J. A., G. A. Badi, L. Franco, and D. Draganov, 2020, Seismic interferometry applied to regional and teleseismic events recorded at Planchón-Peteroa Volcanic Complex, Argentina-Chile: Journal of Volcanology and Geothermal Research, **393**, 106805, doi: 10.1016/j.jvolgeores.2020.106805.

Chamarczuk, M., M. Malinowski, and D. Draganov, 2021, 2D body-wave seismic interferometry as a tool for reconnaissance studies and optimization of passive reflection seismic surveys in hardrock environments: Journal of Applied Geophysics, **187**, 104288, doi: 10.1016/j.jappgeo.2021.104288.

Chamarczuk, M., M. Malinowski, D. Draganov, E. Koivisto, S. Heinonen, and S. Juurela, 2018, Seismic interferometry for mineral exploration: Passive seismic experiment over Kylylahti mine area, Finland: 2nd Conference on Geophysics for Mineral Exploration and Mining, 1–5.

Chamarczuk, M., M. Malinowski, E. Koivisto, S. Heinonen, and S. Juurela, and , COGITO-MIN Working Group, 2017, Passive seismic interferometry for subsurface imaging in an active mine environment: Case study from the Kylylahti Cu-Au-Zn mine, Finland: Decennial Mineral Exploration Conferences, 51–56.

Chen, G., Q. Cheng, Y. Luo, Y. Yang, H. Xu, and X. Deng, 2021, Seismic imaging of the Caosiyao giant porphyry molybdenum deposit using ambient noise tomography: Geophysics, **86**, no. 6, B401–B412, doi: 10.1190/geo2021-0117.1.

Cheraghi, S., J. A. Craven, and G. Bellefleur, 2015, Feasibility of virtual source reflection seismology using interferometry for mineral exploration: A test study in the Lalor Lake volcanogenic massive sulphide mining area, Manitoba, Canada: Geophysical Prospecting, **63**, 833–848, doi: 10.1111/1365-2478.12244.

Curtis, A., H. Nicolson, D. Halliday, J. Trampert, and B. Baptie, 2009, Virtual seismometers in the subsurface of the Earth from seismic interferometry: Nature Geoscience, **2**, 700–704, doi: 10.1038/ngeo615.

Dales, P., L. Pinzon-Ricon, F. Brenguier, P. Boué, N. Arndt, J. McBride, F. Lavoué, C. J. Bean, S. Beaupretre, and R. Fayjaloun, 2020, Virtual sources of body waves from noise correlations in a mineral exploration context: Seismological Research Letters, **91**, 2278–2286, doi: 10.1785/0220200023.

Draganov, D., X. Campman, J. Thorbecke, A. Verdel, and K. Wapenaar, 2009, Reflection images from ambient seismic noise: Geophysics, **74**, no. 5, A63–A67, doi: 10.1190/1.3193529.

Draganov, D., X. Campman, J. Thorbecke, A. Verdel, and K. Wapenaar, 2013, Seismic exploration-scale velocities and structure from ambient seismic noise (> 1 Hz): Journal of Geophysical Research: Solid Earth, **118**, 4345–4360, doi: 10.1002/jgrb.50339.

Draganov, D., R. Ghose, E. Ruigrok, J. Thorbecke, and K. Wapenaar, 2010, Seismic interferometry, intrinsic losses and Q-estimation: Geophysical Prospecting, **58**, 361–373, doi: 10.1111/j.1365-2478.2009.00828.x.

Draganov, D., K. Heller, and R. Ghose, 2012, Monitoring CO_2 storage using ghost reflections retrieved from seismic interferometry: International Journal of Greenhouse Gas Control, **11**, S35–S46, doi: 10.1016/j.ijggc.2012.07.026.

Draganov, D., K. Wapenaar, W. Mulder, J. Singer, and A. Verdel, 2007b, Retrieval of reflections from seismic background-noise measurements: Geophysical Research Letters, **34**, L04305, doi: 10.1029/2006GL028735.

Draganov, D., K. Wapenaar, and J. Thorbecke, 2006, Seismic interferometry: Reconstructing the earth's reflection response: Geophysics, **71**, no. 4, SI61–SI70, doi: 10.1190/1.2209947.

Draganov, D., K. Wapenaar, J. Thorbecke, and O. Nishizawa, 2007a, Retrieving reflection responses by crosscorrelating transmission responses from deterministic transient sources: Application to ultrasonic data: The Journal of the Acoustical Society of America, **122**, EL172–EL178, doi: 10.1121/1.2794864.

Durrheim, R. J., 1986, Recent reflection seismic developments in the Witwatersrand basin, *in* M. Barazangi and L. Brown, eds., Reflection seismology: A global perspective: AGU, 13, 77–83.

Hardage, B. A., 2000, Vertical seismic profiling: Principles, 3rd ed.: Elsevier Science.

Hillers, G., M. Campillo, Y. Ben-Zion, and P. Roux, 2014, Seismic fault zone trapped noise: Journal of Geophysical Research: Solid Earth, **119**, 5786–5799, doi: 10.1002/2014JB011217.

Hollis, D., J. McBride, D. Good, N. Arndt, F. Brenguier, and G. Olivier, 2018, Use of ambient-noise surface-wave tomography in mineral resource exploration and evaluation: 88th Annual International Meeting, SEG, Expanded Abstracts, 1937–1940, doi: 10.1190/segam2018-2998476.1.

Hong, T.-K., and W. Menke, 2006, Tomographic investigation of the wear along the San Jacinto fault, southern California: Physics of the Earth and Planetary Interiors, **155**, 236–248, doi: 10.1016/j.pepi.2005.12.005.

Hurich, C., and S. Deemer, 2013, Combined surface and borehole seismic imaging in a hard rock terrain: A field test of seismic interferometry: Geophysics, **78**, no. 3, B103–B110, doi: 10.1190/geo2012-0325.1.

Jones, H. J., and J. A. Morrison, 1954, Cross-correlation filtering: Geophysics, **19**, 660–683, doi: 10.1190/1.1438036.

Lin, F.-C., M. P. Moschetti, and M. H. Ritzwoller, 2008, Surface wave tomography of the western United States from ambient seismic noise: Rayleigh and Love wave phase velocity maps: Geophysical Journal International, **173**, 281–298, doi: 10.1111/j.1365-246X.2008.03720.x.

Lin, F.-C., M. H. Ritzwoller, J. Townend, S. Bannister, and M. K. Savage, 2007, Ambient noise Rayleigh wave tomography of New Zealand: Geophysical Journal International, **170**, 649–666, doi: 10.1111/j.1365-246X.2007.03414.x.

Liu, Q., X. Feng, C. Liu, M. Zhang, Y. Tian, and H. Hou, 2022, Metallic mineral exploration by using ambient noise tomography in Ashele copper mine, Xinjiang, China: Geophysics, **87**, no. 3, B221–B231, doi: 10.1190/geo2020-0923.1.

Liu, Y., D. Draganov, K. Wapenaar, and B. Arntsen, 2016, Retrieving virtual reflection responses at drill-bit positions using seismic interferometry with drill-bit noise: Geophysical Prospecting, **64**, 348–360, doi: 10.1111/1365-2478.12292.

Liu, Y., K. Wapenaar, J. van der Neut, and B. Arntsen, 2014, Combining inter-source seismic interferometry and source-receiver interferometry for deep local imaging: 84th Annual International Meeting, SEG, Expanded Abstracts, 5107–5112, doi: 10.1190/segam2014-1111.1.

Löer, K., G. A. Meles, A. Curtis, and I. Vasconcelos, 2014, Diffracted and pseudo-physical waves from spatially limited arrays using source-receiver interferometry (SRI): Geophysical Journal International, **196**, 1043–1059, doi: 10.1093/gji/ggt435.

Malehmir, A., and G. Bellefleur, 2009, 3D seismic reflection imaging of volcanic-hosted massive sulfide deposits: Insights from reprocessing Halfmile Lake data, New Brunswick, Canada: Geophysics, **74**, no. 6, B209–B219, doi: 10.1190/1.3230495.

Manzi, M. S., M. A. Gibson, K. A. Hein, N. King, and R. J. Durrheim, 2012, Application of 3D seismic techniques to evaluate ore resources in the West Wits Line goldfield and portions of the West Rand goldfield, South Africa: Geophysics, **77**, no. 5, WC163–WC171, doi: 10.1190/geo2012-0133.1.

Mehta, K., A. Bakulin, J. Sheiman, R. Calvert, and R. Snieder, 2007, Improving the virtual source method by wavefield separation: Geophysics, **72**, no. 4, V79–V86, doi: 10.1190/1.2733020.

Meles, G. A., K. Löer, M. Ravasi, A. Curtis, and C. A. da Costa Filho, 2015, Internal multiple prediction and removal using Marchenko autofocusing and seismic interferometry: Geophysics, **80**, no. 1, A7–A11, doi: 10.1190/geo2014-0408.1.

Melo, G., A. Malcolm, D. Mikesell, and K. van Wijk, 2013, Using SVD for improved interferometric Green's function retrieval: Geophysical Journal International, **194**, 1596–1612, doi: 10.1093/gji/ggt172.

Milkereit, B., D. Eaton, J. Wu, G. Perron, M. H. Salisbury, E. K. Berrer, and G. Morrison, 1996, Seismic imaging of massive sulfide deposits; Part II, Reflection seismic profiling: Economic Geology, **91**, 829–834, doi: 10.2113/gsecongeo.91.5.829.

Miyazawa, M., R. Snieder, and A. Venkataraman, 2008, Application of seismic interferometry to extract P- and S-wave propagation and observation of shear-wave splitting from noise data at Cold Lake, Alberta, Canada: Geophysics, **73**, no. 4, D35–D40, doi: 10.1190/1.2937172.

Nakata, N., 2016, Near-surface S-wave velocities estimated from traffic-induced Love waves using seismic interferometry with double beamforming: Interpretation, **4**, no. 4, SQ23–SQ31, doi: 10.1190/INT-2016-0013.1.

Nakata, N., R. Snieder, T. Tsuji, K. Larner, and T. Matsuoka, 2011, Shear wave imaging from traffic noise using seismic interferometry by cross-coherence: Geophysics, **76**, no. 6, SA97–SA106, doi: 10.1190/geo2010-0188.1.

Nishitsuji, Y., E. Ruigrok, M. Gomez, K. Wapenaar, and D. Draganov, 2016, Reflection imaging of aseismic zones of the Nazca slab by global-phase seismic interferometry: Interpretation, **4**, no. 3, SJ1–SJ16, doi: 10.1190/INT-2015-0225.1.

Olivier, G., F. Brenguier, M. Campillo, R. Lynch, and P. Roux, 2015, Body-wave reconstruction from ambient seismic noise correlations in an underground mine: Geophysics, **80**, no. 3, KS11–KS25, doi: 10.1190/geo2014-0299.1.

Perron, V., A. Laurendeau, F. Hollender, P.-Y. Bard, C. Gélis, P. Traversa, and S. Drouet, 2018, Selecting time windows of seismic phases and noise for engineering seismology applications: A versatile methodology and algorithm: Bulletin of Earthquake Engineering, **16**, 2211–2225, doi: 10.1007/s10518-017-0131-9.

Place, J., D. Draganov, A. Malehmir, C. Juhlin, and C. Wijns, 2019, Cross-coherence-based interferometry for the retrieval of first arrivals and subsequent tomographic imaging of differential weathering: Geophysics, **84**, no. 4, Q37–Q48, doi: 10.1190/geo2018-0405.1.

Poliannikov, O. V., and M. E. Willis, 2011, Interferometric correlogram-space analysis: Geophysics, **76**, no. 1, SA9–SA17, doi: 10.1190/1.3519875.

Polychronopoulou, K., A. Lois, and D. Draganov, 2020, Body-wave passive seismic interferometry revisited: Mining exploration using the body waves of local microearthquakes: Geophysical Prospecting, **68**, 232–253, doi: 10.1111/1365-2478.12884.

Pretorius, C. C., M. A. Gibson, and Q. Snyman, 2011, Development of high resolution 3D vertical seismic profiles: Journal of the Southern African Institute of Mining and Metallurgy, **111**, 117–125.

Quiros, D. A., L. D. Brown, A. Cabolova, C. Chen, K. K. Davenport, J. Hole, L. Han, M. C. Chapman, and W. Mooney, 2015b, Reflection imaging using earthquake sources: A novel application of reverse vertical seismic profiling (RVSP): 85th Annual International Meeting, SEG, Expanded Abstracts, 5565–5569, doi: 10.1190/segam2015-5931898.1.

Quiros, D. A., L. D. Brown, K. K. Davenport, J. A. Hole, A. Cabolova, C. Chen, L. Han, M. C. Chapman, and W. D. Mooney, 2017, Reflection imaging with earthquake sources and dense arrays: Journal of Geophysical Research: Solid Earth, **122**, 3076–3098, doi: 10.1002/2016JB013677.

Quiros, D. A., L. D. Brown, and D. Kim, 2016, Seismic interferometry of railroad induced ground motions: Body and surface wave imaging: Geophysical Journal International, **205**, 301–313, doi: 10.1093/gji/ggw033.

Quiros, D. A., A. Cabolova, L. D. Brown, C. Chen, J. E. Ebel, and J. Starr, 2015a, Aftershock imaging with dense arrays (AIDA) following the Mw 4.0 Waterboro earthquake of 16 October 2012 Maine, U.S.A: Seismological Research Letters, **86**, 1032–1039, doi: 10.1785/0220140169.

Saengduean, P., M. P. Moschetti, and R. Snieder, 2021, Inter-source interferometry of seismic body waves: Required conditions and examples: Pure and Applied Geophysics, **178**, 3441–3460, doi: 10.1007/s00024-021-02814-y.

Schuster, G. T., J. Yu, J. Sheng, and J. Rickett, 2004, Interferometric/daylight seismic imaging: Geophysical Journal International, **157**, 838–852, doi: 10.1111/j.1365-246X.2004.02251.x.

Shapiro, N. M., M. Campillo, L. Stehly, and M. H. Ritzwoller, 2005, High-resolution surface-wave tomography from ambient seismic noise: Science, **307**, 1615, doi: 10.1126/science.1108339.

Snieder, R., 2004, Extracting the Green's function from the correlation of coda waves: A derivation based on stationary phase: Physical Review E, **69**, 46610, doi: 10.1103/PhysRevE.69.046610.

Tonegawa, T., and K. Nishida, 2010, Inter-source body wave propagations derived from seismic interferometry: Geophysical Journal International, **183**, 861–868, doi: 10.1111/j.1365-246X.2010.04753.x.

van Manen, D.-J., J. O. Robertsson, and A. Curtis, 2005, Modeling of wave propagation in inhomogeneous media: Physical Review Letters, **94**, 164301, doi: 10.1103/PhysRevLett.94.164301.

Wapenaar, K., 2004, Retrieving the elastodynamic Green's function of an arbitrary inhomogeneous medium by cross correlation: Physical Review Letters, **93**, 254301, doi: 10.1103/PhysRevLett.93.254301.

Youzwishen, C. F., and G. F. Margrave, 1999, Finite difference modeling of acoustic waves in Matlab: The 11th Annual Research Report of the CREWES Project, 1–4.

Zhan, Z., S. Ni, D. V. Helmberger, and R. W. Clayton, 2010, Retrieval of Moho-reflected shear wave arrivals from ambient seismic noise: Geophysical Journal International, **182**, 408–420, doi: 10.1111/j.1365-246X.2010.04625.x.

Zhang, H., F. Wang, R. Myhill, and H. Guo, 2019, Slab morphology and deformation beneath Izu-Bonin: Nature Communications, **10**, 1–8, doi: 10.1038/s41467-019-09279-7.

Biographies and photographs of the authors are not available.